

**Balanced electron and hole transfer behavior enables approaching 19%
efficiency thick-film organic solar cells with improved fill factor**

Zhongwei Ge^{1,2}, Jiawei Qiao³, Xiaoming Li², Runzheng Gu³, Wenqing Zhang³,
Bohao Song⁴, Guanghao Lu⁴, Wei Ma⁵, Xiaotao Hao^{3*}, Yanming Sun^{1,2*}

¹Hangzhou International Innovation Institute, Beihang University, Hangzhou 311115,
P. R. China.

²School of Chemistry, Beihang University, Beijing 100191, P. R. China.

³School of Physics State Key Laboratory of Crystal Materials, Shandong University,
Jinan 250100, P. R. China.

⁴State Key Laboratory of Electrical Insulation and Power Equipment, Xi'an Jiaotong
University, Xi'an 710054, P. R. China

⁵State Key Laboratory for Mechanical Behavior of Materials, Xi'an Jiaotong
University, Xi'an 710049, P. R. China

E-mail: sunym@buaa.edu.cn; haoxt@sdu.edu.cn

Methods

Materials. PM6 and L8-BO were purchased from Solarmer Materials (Beijing, China). DTY-2F was synthesized in our group. P(o-tol)₃ was purchased from Energy Chemical and Pd₂(dba)₃ was purchased from Leyan.com. [2-(9H-Carbazol-9-yl)ethyl] phosphonic acid (2PACz) was purchased from Aladdin. All purchased materials were used without further purification.

Device fabrication. Organic solar cells were fabricated with a conventional structure of ITO/2PACz/Active layer/PNDIT-F3N/Ag. ITO substrates were treated in detergent, deionized water, acetone and isopropanol for 15 min via the ultrasonic method and then dried in an oven for 2 hours. The precleaned substrates were treated with plasma for 2 min, then 2PACz (0.3 mg mL⁻¹ in ethanol) was spin-cast on top of ITO surface at 3000 rpm for 30 s and annealed at 100 °C for 8 min. PM6 and L8-BO solution were dissolved in chloroform solvent with concentration of 15 mg/ml and 21 mg/ml, respectively. For devices with PM6+DYT-2F/L8-BO, PM6 and DYT-2F were dissolved in chloroform with a weight ratio of 1:0.1. In the case of D18/L8-BO, D18 was dissolved in chlorobenzene with a concentration of 12 mg/ml and L8-BO solution is prepared as mentioned above. 0.5% DIO was used as the solvent additive for acceptor solution. To prepare OSCs with different thickness, the donor and acceptor solution were spin-cast on 2PACz surface in sequency at rotation rate of 3200/2000 rpm (90/210 nm), 2600/2600 rpm (120/180 nm), 2000/3200 rpm (150/150 nm), and 1500/4000 rpm (180/120 nm), respectively. For the fabrication of blade-coated PM6+DYT-2F/L8-BO films, the platform needs to be continuously heated at 50 °C. PM6+DYT-2F solution (w/w, 16 mg/mL in o-xylene) was blade-coated onto the 2PACz-coated substrates with a speed of 22 mm/s and then annealed for 1 min. The L8-BO solution (22 mg/mL in o-xylene) was blade-coated on top of donor layer with a speed of 29 mm/s. Subsequently, the active layer was thermal annealed at 80 °C for 8 min, PNDIT-F3N solution dissolved in methanol and acetic acid (200:1) with a concentration of 1.2 mg/ml was spin-cast on the active layer at 4200 rpm for 30 s. Finally, the Ag electrode (110 nm) was deposited by thermal evaporation under vacuum condition of $\sim 3 \times 10^{-4}$ Pa.

Device measurement. The $J-V$ curves were measured from -0.5 to 1 V with a scan step of 50 mV

and a dwell time of 10 ms, along the forward scan direction, using a Keithley 2400 Source Measure Unit. The photovoltaic performance of all the OSCs was measured in a N₂-filled glove box at room temperature (ca. 25 Celsius degree) using an Air Mass 1.5 Global (AM 1.5 G) solar simulator (SS-F5-3A, Enlitech) with an irradiation intensity of 100 mW cm⁻², which was measured by a calibrated silicon solar cell (SRC2020, Enlitech). The $J-V$ curves were measured from -0.5 to 1 V with a scan step of 50 mV and a dwell time of 10 ms in a forward scan direction by using a Keithley 2400 Source Measure Unit. EQE spectra were measured by using a solar-cell spectral-response measurement system (QE-R3011, Enlitech). The active area of devices is 5.12 mm². The devices were tested through a mask with an area of 3.152 mm².

Exciton diffusion length measurements. In general, the equation of $L_D = \sqrt{D\tau}$ (τ represents exciton lifetime and D is the diffusion constant) is used to calculate the diffusion length. Increasing fluence densities can accelerate decay of GSB signals, which is attributed to the exciton-exciton annihilation (EEA). When the bimolecular recombination is considered, the dynamic decay of excitons can be described as follows

$$\frac{dn(t)}{dt} = -kn(t) - \frac{1}{2}\gamma n^2(t)$$

with the solution of

$$n(t) = \frac{n(0)e^{-kt}}{1 + \frac{\gamma}{2k}n(0)[1 - e^{-kt}]}$$

where $n(t)$ is the exciton density as a function of delay time, $k = 1/\tau$ is the monomolecular decay rate constant, and γ is the bimolecular recombination rate constant aroused from EEA. Next, the 3D

exciton diffusion coefficient was estimated by using the formula of $D = \frac{\gamma}{8\pi R}$, where R is the radius of EEA.

Trap density measurement. The defects density can be calculated from capacitance spectroscopy measurement in dark environment. The frequency axis can be scaled to energy axis as the follows

$$E_{\omega} = kT \ln \left(\frac{2\nu_0}{\omega} \right)$$

where ω is the angular frequency calculated by $\omega = 2\pi f$, ν_0 is the attempt-to-escape frequency of 10^9 Hz, k is the Boltzmann constant, T is the thermodynamic temperature. The trap density at energy E_{ω} can be acquired as

$$N_t(E_{\omega}) = -\frac{V_{bi}dC_{\omega}}{qd_{\omega}kT}$$

d is the thickness of the active layer and V_{bi} is the built-in voltage measured through Mott–Schottky characterization. Then the energy distribution for the density of states (DoS) can be described with Gaussian shape distribution

$$N_t(E) = \frac{N_t}{\sqrt{2\pi}\sigma} \exp \left[-\frac{(E_t - E)^2}{2\sigma^2} \right]$$

where N_t is the total density, E_t is the center of the DoS, σ is the disorder parameter.

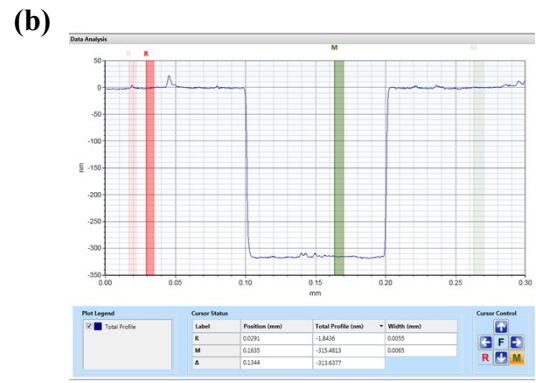
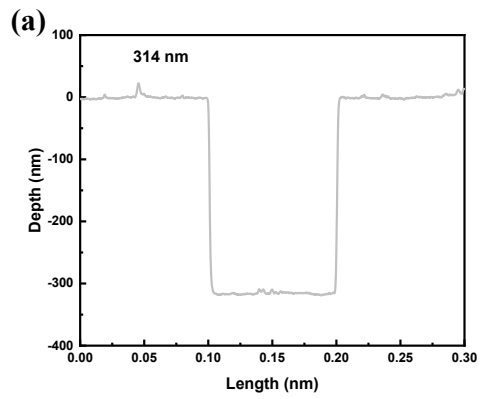
Time-Resolved Photoluminescence (TRPL) Spectra Measurement. The TRPL spectra measurements were performed through a laser-scanned confocal imaging microscopy (Nanofinder FLEX2, Tokyo Instruments, Inc.) combined with a time-correlated single-photon counting (TCSPC) module (Becker & Hickl, SPC-150). The 800 nm pulsed laser was focused by an objective lens (50 \times) into a near diffraction-limited spot to excite the samples. A neutral density filter coupled with a power meter was used to regulate the excitation density at samples. The fluorescence signals were collected by the high-resolution detectors. Herein, the appropriate optical filters were employed to realize excitonic PL collection with > 800 nm for “edge state” emission. Furthermore, the two-dimensional (2D) TRPL scanning consists of 6 32×32 pixels. The samples were encapsulated in a high-purity N_2 -filled glove box for TRPL measurements.

Steady-state and ultrafast transient absorption (TA) spectroscopy. The steady-state absorption spectra of the samples were recorded on an Agilent Cary 5000 spectrophotometer. Femtosecond transient absorption spectroscopy is based on an Ultrafast Helios pump-probe optical system (the nonlinear frequency mixing techniques, a fiber-coupled multichannel spectrometer and so on) combined with a regenerative amplified Ti:sapphire laser system from Coherent (800 nm, 100 fs, 7

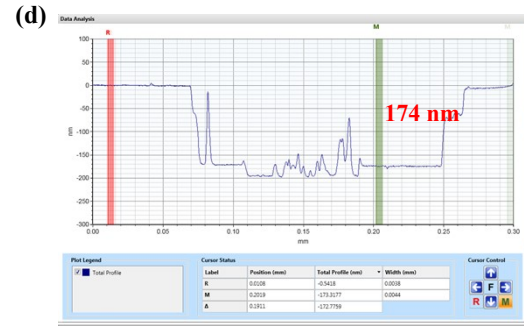
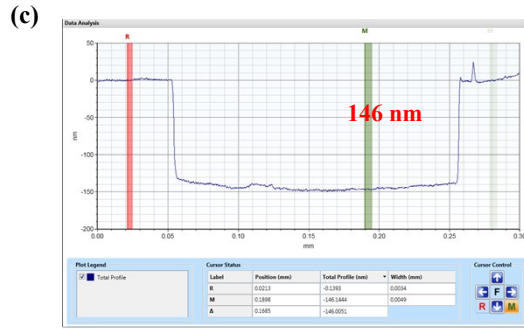
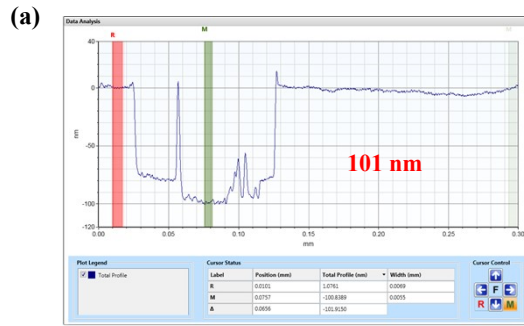
mJ/pulse and 1 KHz repetition rate). The delay between pump and probe pulses can be controlled by a motorized delay stage, leading to a maximum delay time of 8 ns. The intensity of pump pulse can be tailored by a variable neutral density filter wheel and measured by a power meter. The samples were encapsulated in a high-purity N₂-filled glove box for TA measurements.

Atomic force microscopy (AFM) and grazing incidence wide-angle X-ray scattering (GIWAXS) measurement. AFM measurements were performed on a Dimension Icon AFM (Bruker) in a tapping mode under ambient conditions. Grazing incident wide-angle X-ray scattering (GIWAXS) measurements were conducted at beamline 7.3.3 at the Advanced Light Source (samples were prepared on Si substrates using identical preparation conditions as those used in devices). The X-ray beam was incident at a grazing angle from 0.12° to 0.16°. The X-ray data was supported by the Director, Office of Science, Office of Basic Energy Sciences, of the U.S. Department of Energy under Contract No. DE-AC02-05CH11231. The authors thank Chenhui Zhu at beamline 7.3.3 for assistance with data acquisition. Resonant Soft X-ray Scattering (RSoXS) transmission measurements were performed at beamline 11.0.1.2 at the Advanced Light Source (ALS). (Samples for were prepared on a PSS modified Si substrate under the same conditions as those used for device fabrication, and then transferred by floating in water to a 1.5 mm × 1.5 mm, 100 nm thick Si₃N₄ membrane supported by a 5 mm × 5 mm, 200 μm thick Si frame (Norcada Inc.). 2-D scattering patterns were collected on an in-vacuum CCD camera (Princeton Instrument PI-MTE). The sample detector distance was calibrated from diffraction peaks of a triblock copolymer poly(isoprene-*b*-styrene-*b*-2-vinyl pyridine), which has a known spacing of 391 Å. The beam size at the sample is approximately 100 μm by 200 μm).

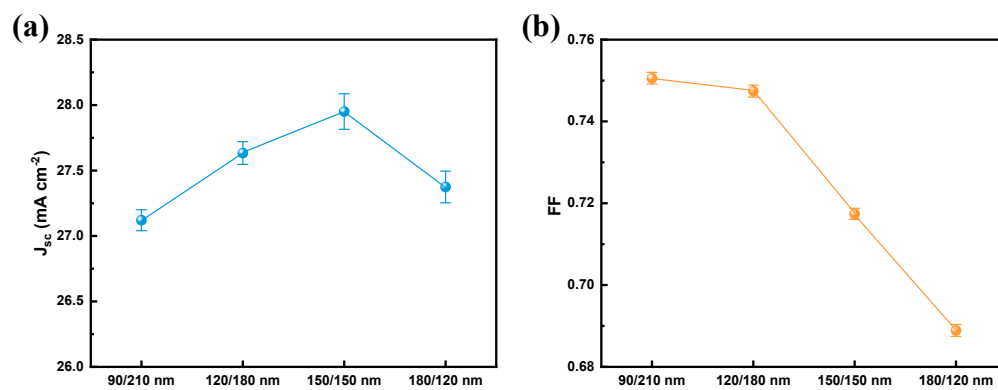
Ultraviolet-visible (UV-vis) spectroscopy measurement. UV-vis absorption spectra of the pristine and blend films were acquired with a UV-vis spectrophotometer (Shimadzu UV-3700).



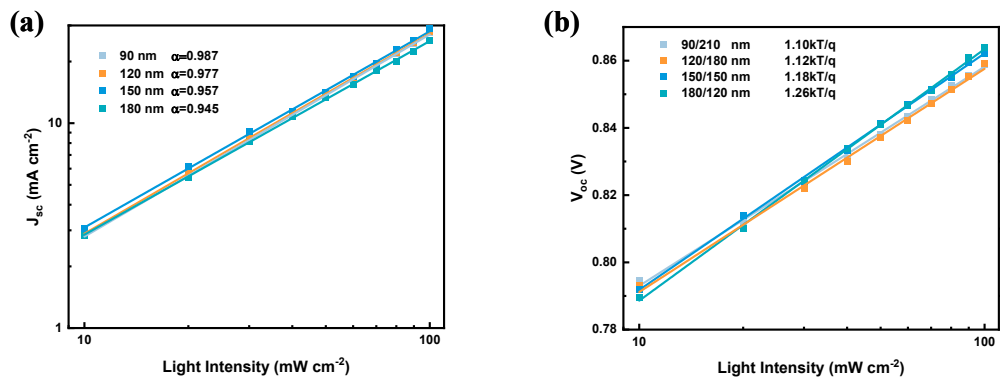
Supplementary Figure 1. Thickness results of 314 nm films from a surface profilometer.



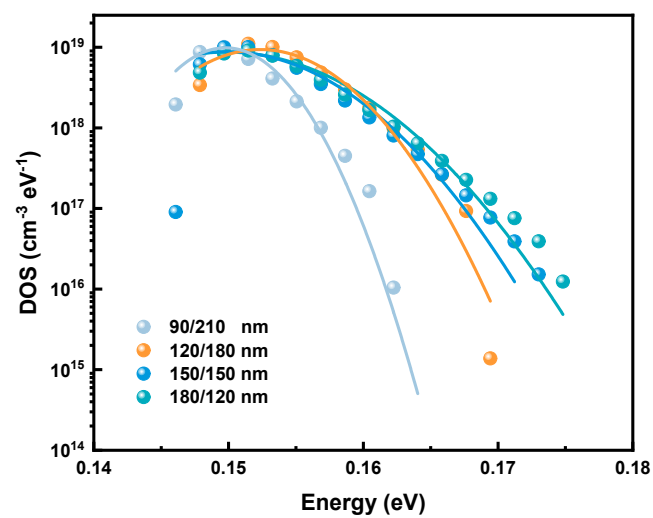
Supplementary Figure 2. Thickness results of 101 nm, 126 nm, 146 nm, and 174 nm films from a surface profilometer.



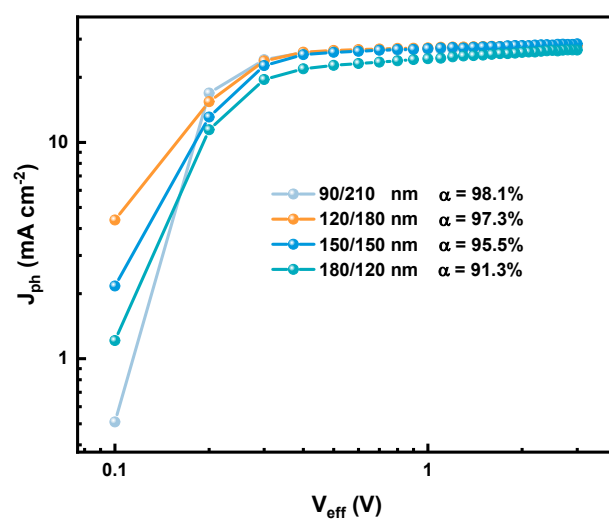
Supplementary Figure 3. The variation of J_{sc} and FF values with different donor and acceptor layer thicknesses (Error bars represent the standard error of the mean ($n = 20$)).



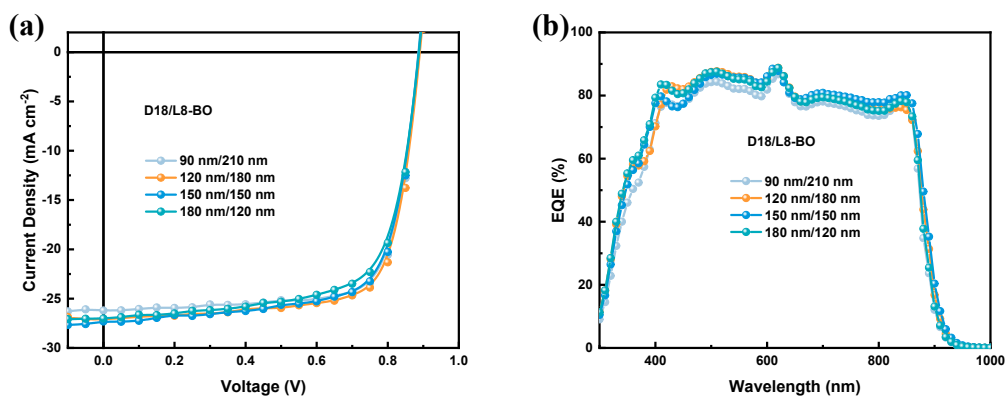
Supplementary Figure 4. (a) J_{sc} and (b) V_{oc} versus light intensity characteristics of PM6/L8-BO devices fabricated with different donor layer thicknesses (the total thickness of active layer for devices is 300 nm).



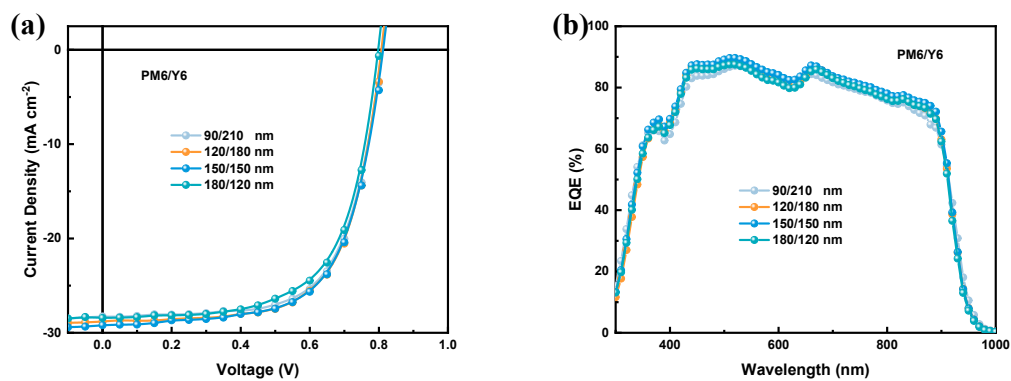
Supplementary Figure 5. The plots of DoS as a function of energy and corresponding Gaussian fitting curves for PM6/L8-BO devices with different donor and acceptor layer thicknesses.



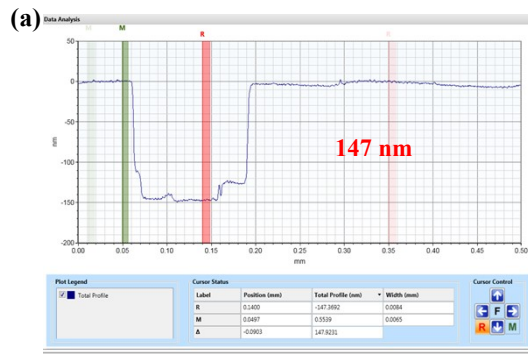
Supplementary Figure 6. The photocurrent density (J_{ph}) versus effective voltage (V_{eff}) characteristics of PM6/L8-BO devices fabricated with different donor and acceptor layer thicknesses.



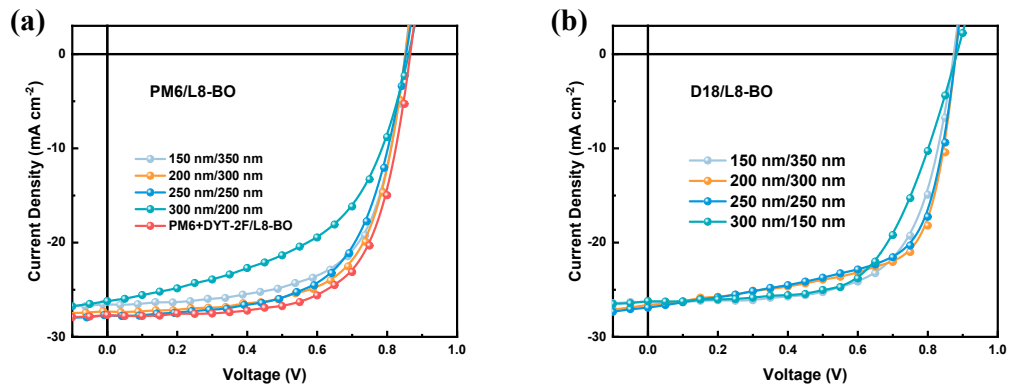
Supplementary Figure 7. (a) $J-V$ curves and (b) corresponding EQE spectra for D18/L8-BO devices fabricated with different donor and acceptor layer thicknesses.



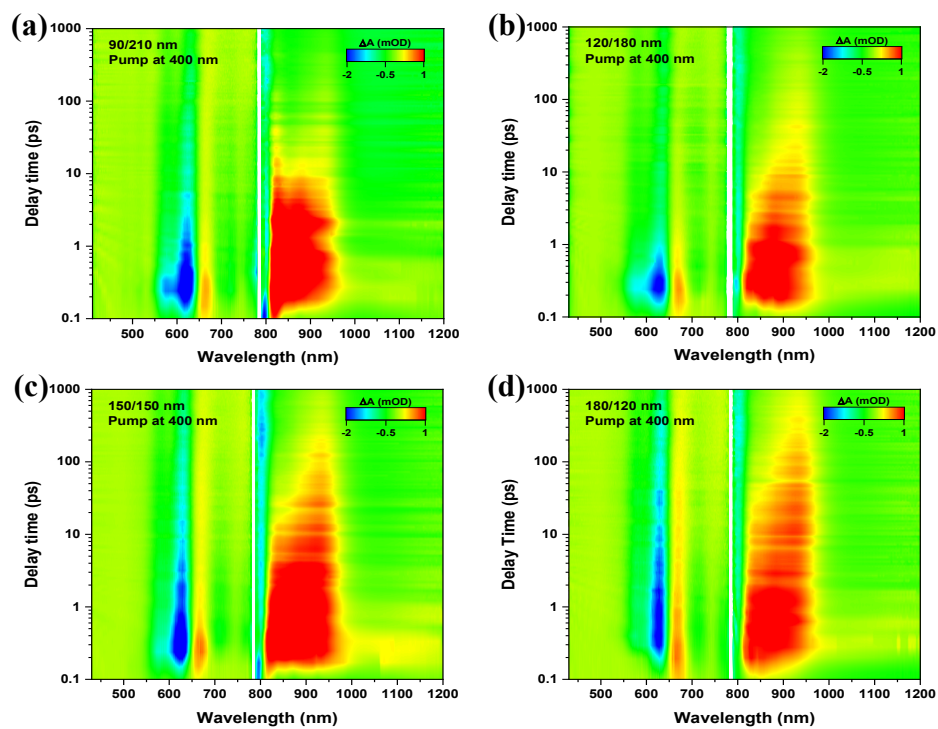
Supplementary Figure 8. (a) $J-V$ curves and (b) corresponding EQE spectra for PM6/Y6 devices fabricated with different donor and acceptor layer thicknesses.



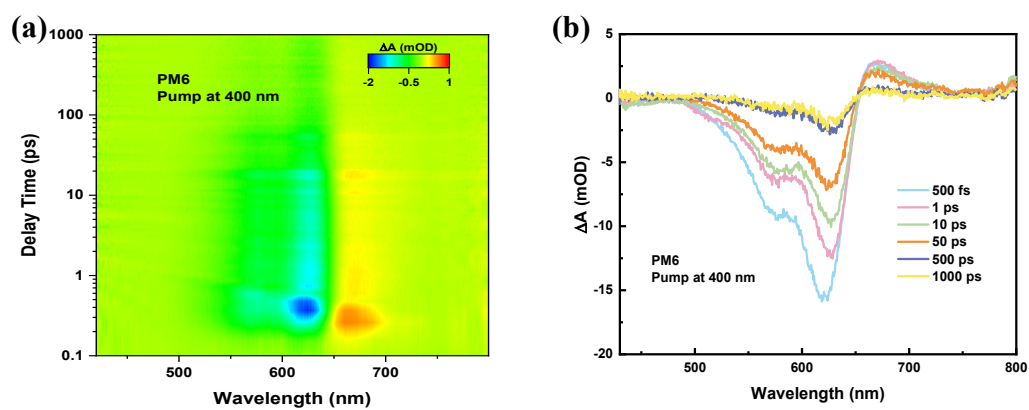
Supplementary Figure 9. Thickness results of 147 nm, 205 nm, 253 nm, and 293 nm films from a surface profilometer.



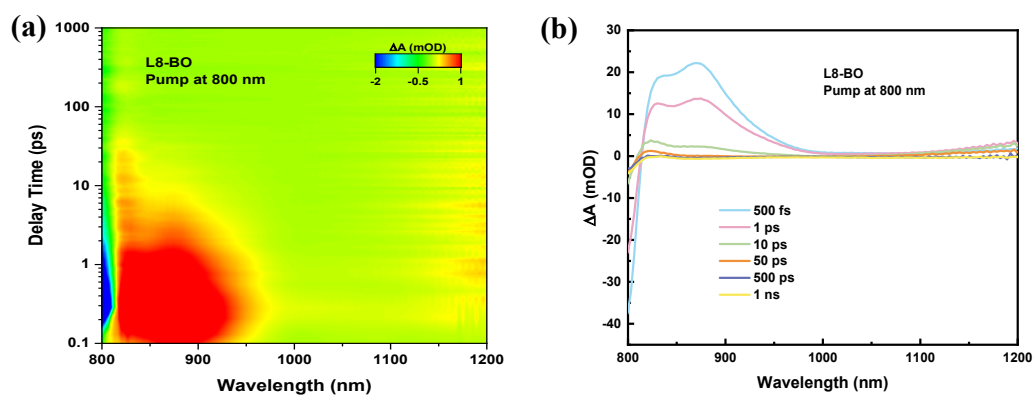
Supplementary Figure 10. J - V curves for binary and ternary devices with total thickness of 500 nm.



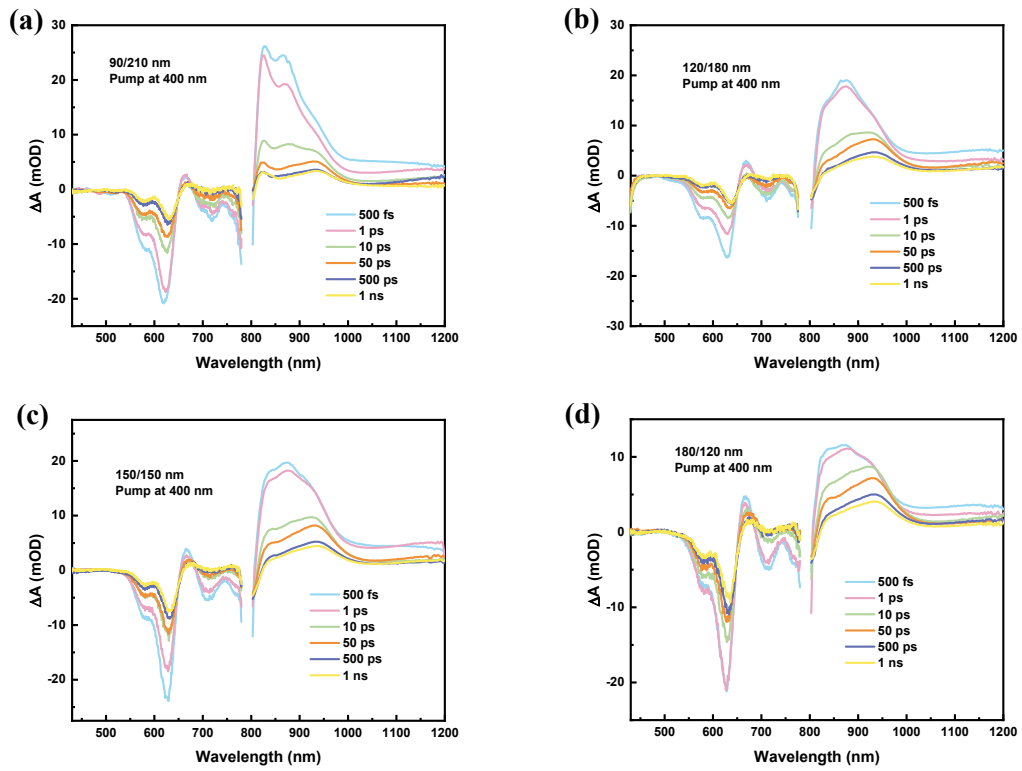
Supplementary Figure 11. (a)-(d) 2D TAS image of PM6/L8-BO films with different donor and acceptor layer thicknesses pumped at 400 nm.



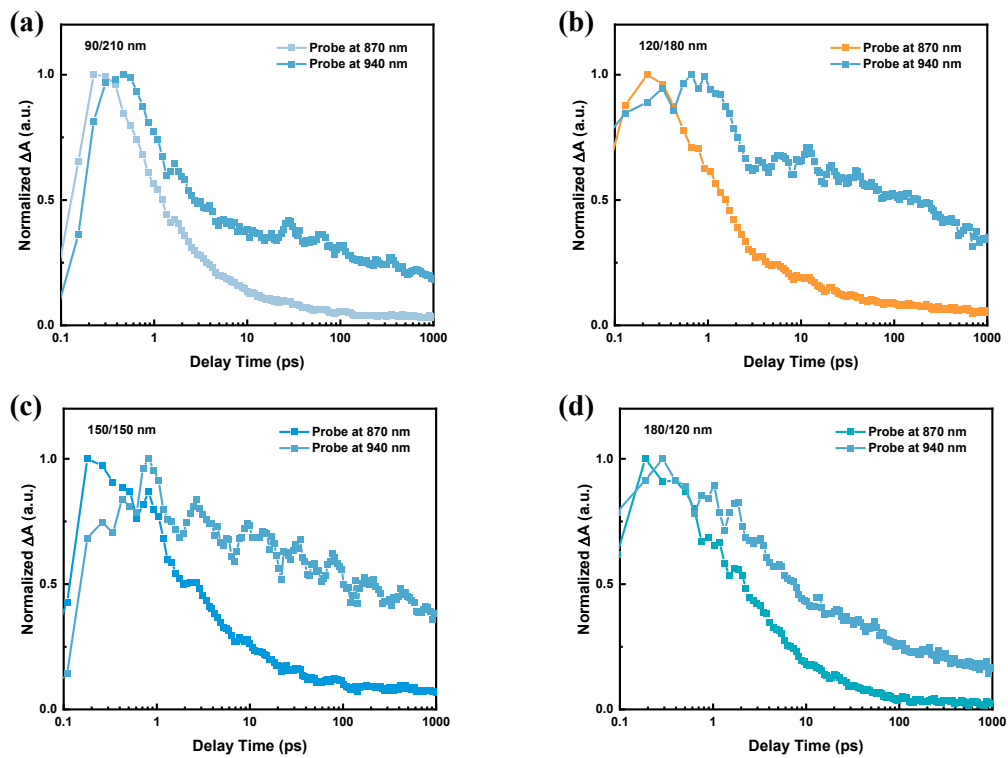
Supplementary Figure 12. (a) 2D TAS image and (b) the corresponding TAS spectra of PM6 neat film over time.



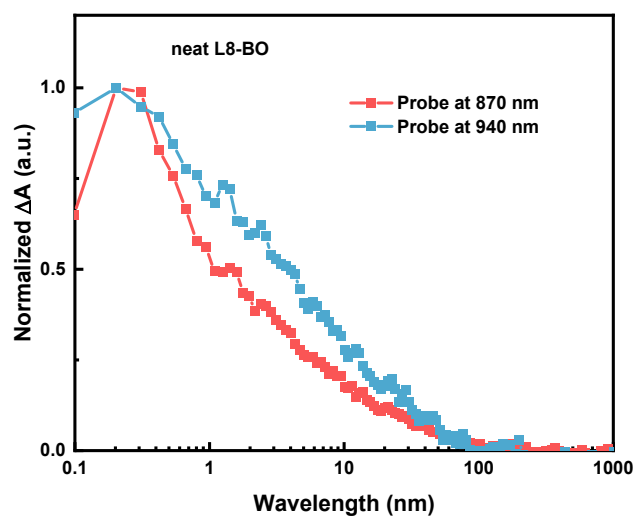
Supplementary Figure 13. (a) 2D TAS image and (b) the corresponding TAS spectra of L8-BO neat film over time.



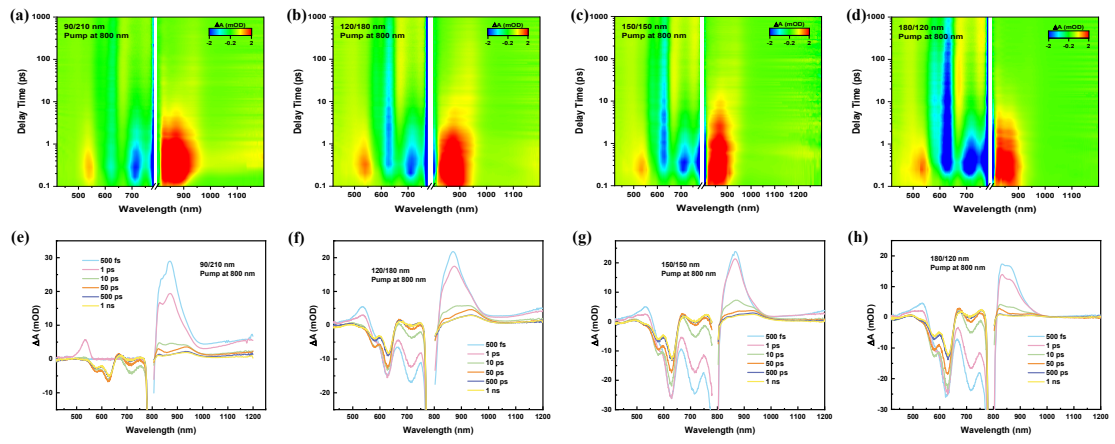
Supplementary Figure 14. (a)-(d) The TAS spectra of PM6/L8-BO thick films with different donor and acceptor layer thicknesses over time.



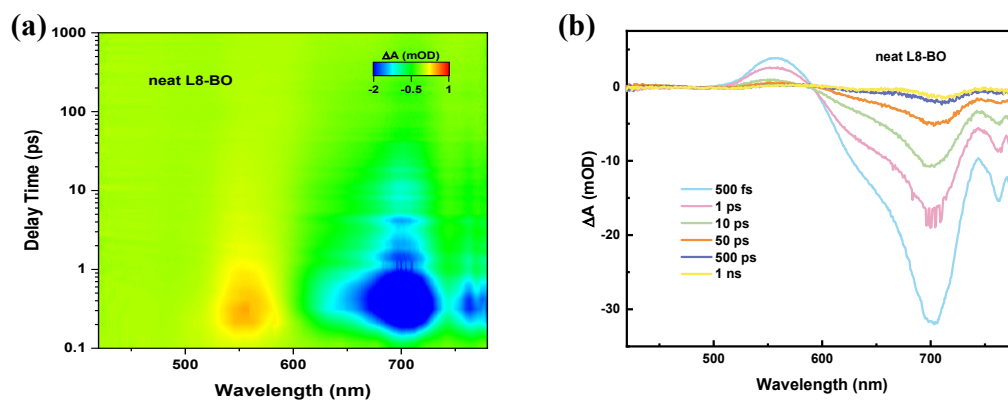
Supplementary Figure 15. (a)-(d) Normalized TAS dynamic curves probed at 870 nm and 940 nm for PM6/L8-BO thick films with different donor and acceptor layer thicknesses.



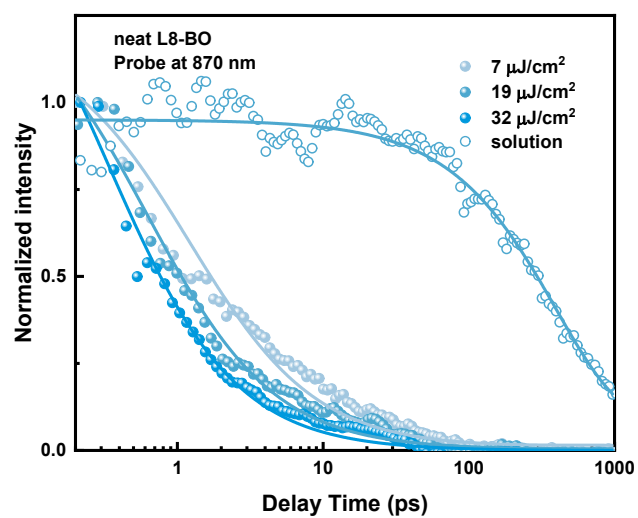
Supplementary Figure 16. Normalized TAS dynamic curves probed at 870 nm and 940 nm for L8-BO neat film.



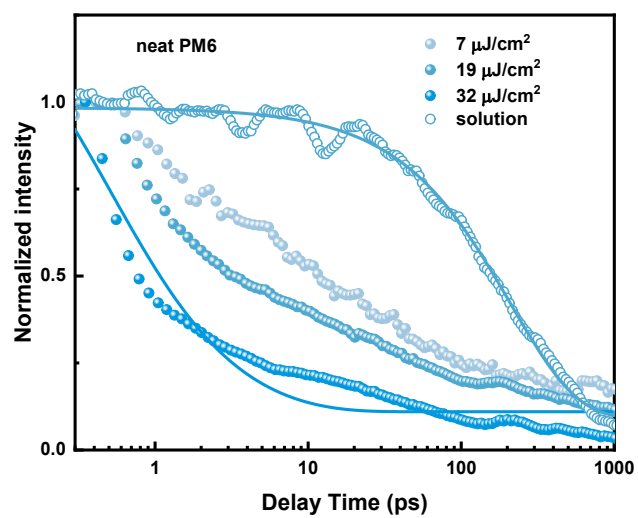
Supplementary Figure 17. (a)-(d) 2D TAS image and (e)-(f) the corresponding TAS spectra of PM6/L8-BO films with different donor and acceptor layer thicknesses pumped at 800 nm over time.



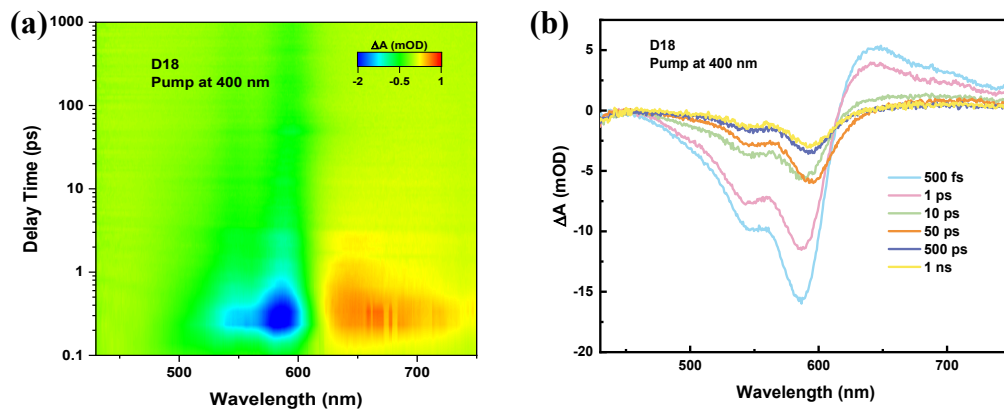
Supplementary Figure 18. (a) 2D TAS image and (b) the corresponding TAS spectra of L8-BO neat film probed at the visible light range.



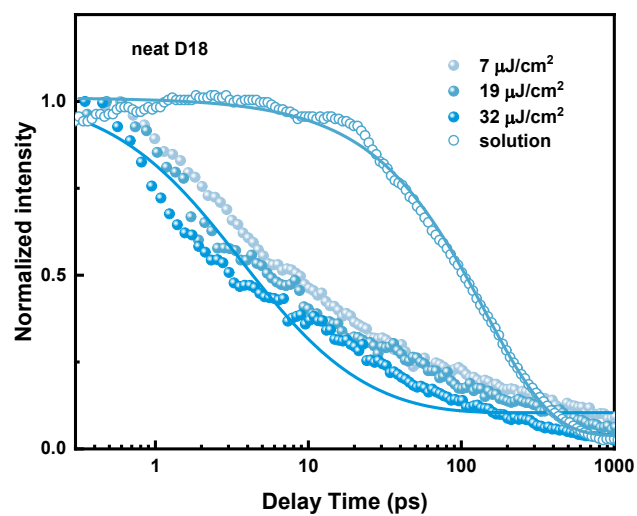
Supplementary Figure 19. Dynamic profiles of singlet excitons of L8-BO pumped at different fluence densities.



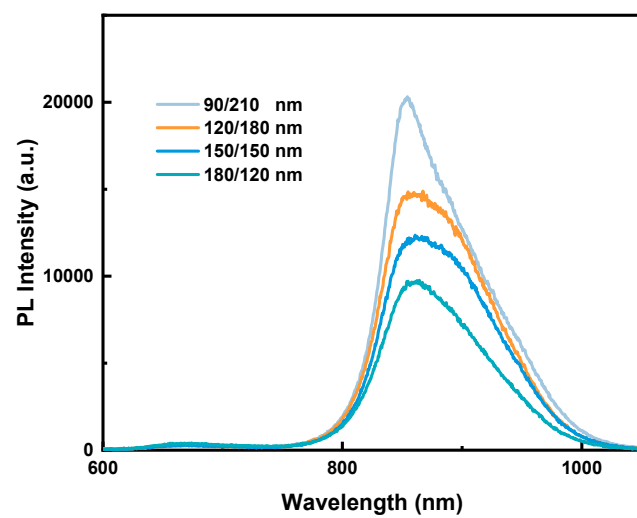
Supplementary Figure 20. Dynamic profiles of singlet excitons of PM6 pumped at different fluence densities.



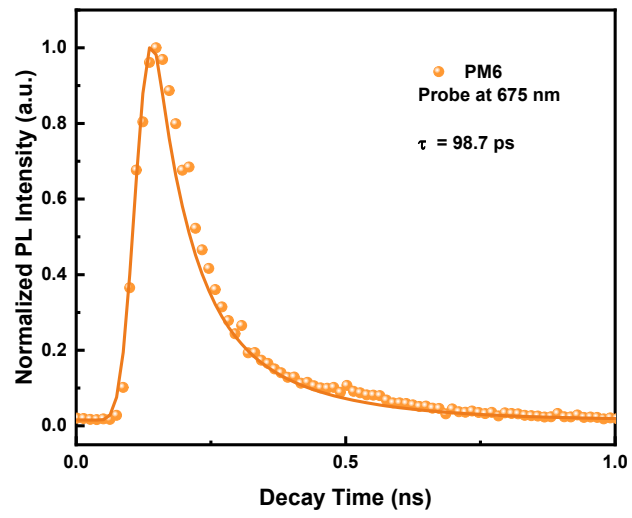
Supplementary Figure 21. (a) 2D TAS image and (b) the corresponding TAS spectra of D18 neat film over time.



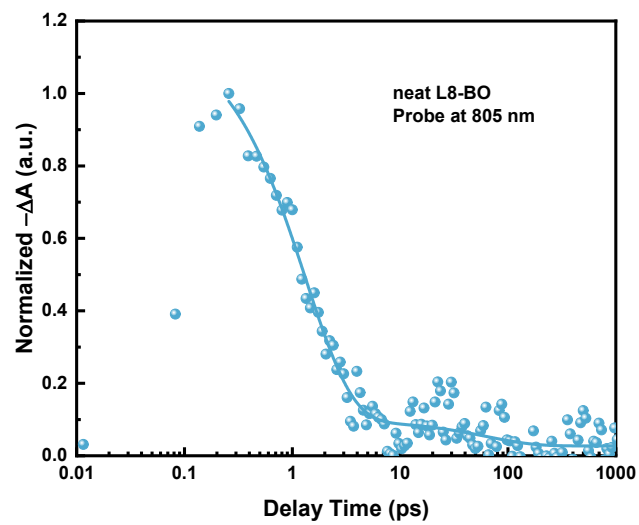
Supplementary Figure 22. Dynamic profiles of singlet excitons of D18 pumped at different fluence densities.



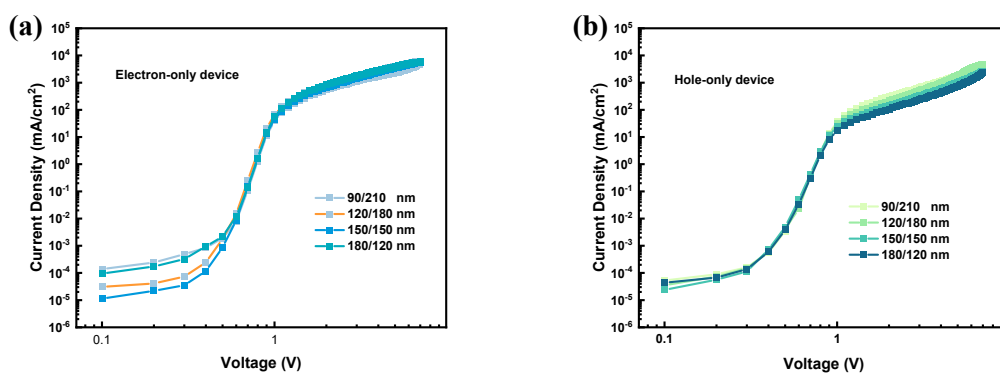
Supplementary Figure 23. Steady-state PL spectra of PM6/L8-BO blend films with different donor and acceptor layer thicknesses.



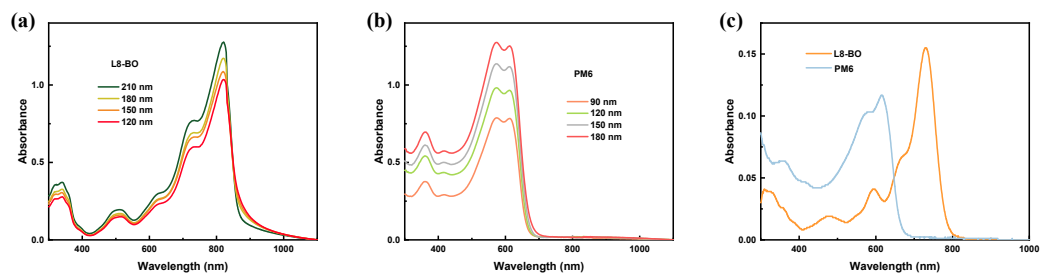
Supplementary Figure 24. Normalized TRPL spectra of PM6 neat film probed at 675 nm.



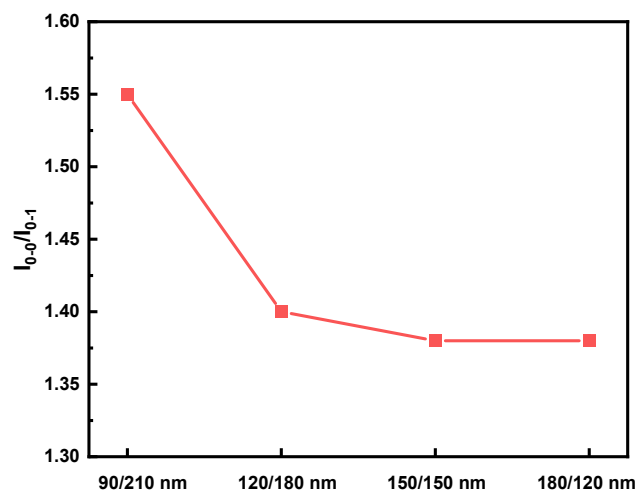
Supplementary Figure 25. Normalized decay curves probed at 805 nm for L8-BO neat film pumped at 800 nm.



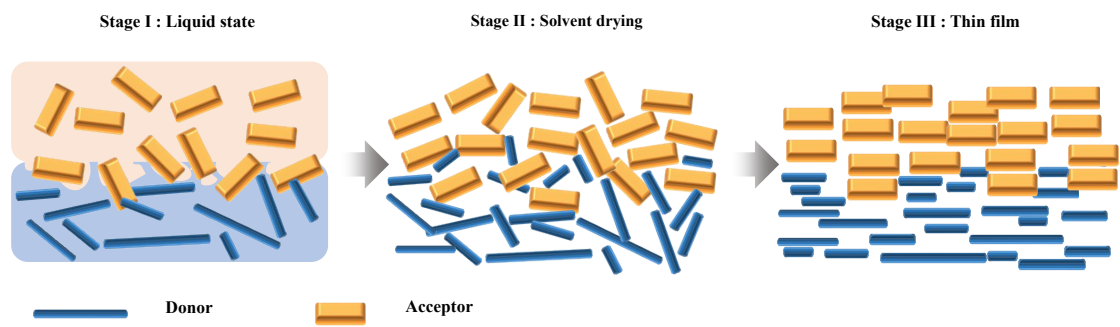
Supplementary Figure 26. SCLC curves of (a) electron-only devices and (b) hole-only devices for PM6/L8-BO thick-film OSCs with different donor and acceptor layer thicknesses.



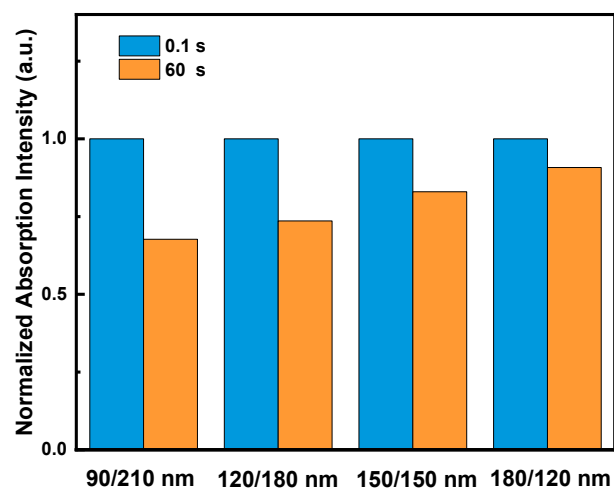
Supplementary Figure 27. UV-vis absorption spectra for (a) L8-BO film and (b) PM6 film with different thicknesses. (c) UV-vis absorption spectra of PM6 and L8-BO in chloroform solution with same concentration.



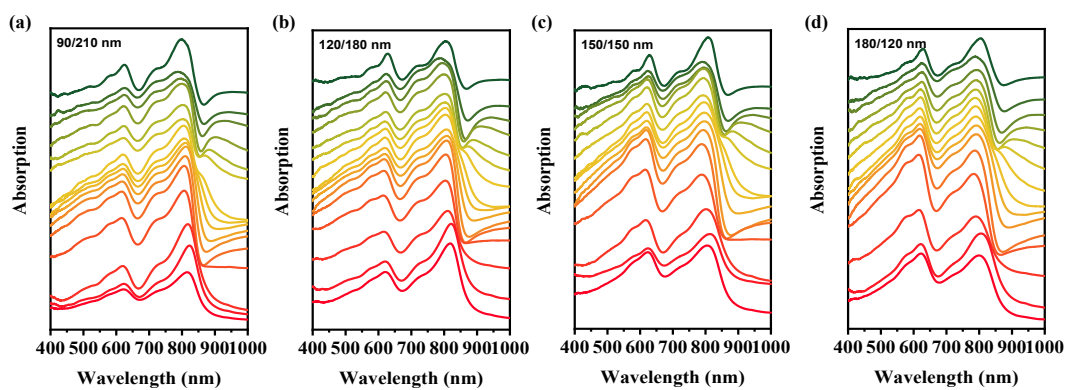
Supplementary Figure 28. The absorption intensity ratio of 0-0 peak and 0-1 peak for PM6/L8-BO blend thick film with different donor and acceptor layer thicknesses.



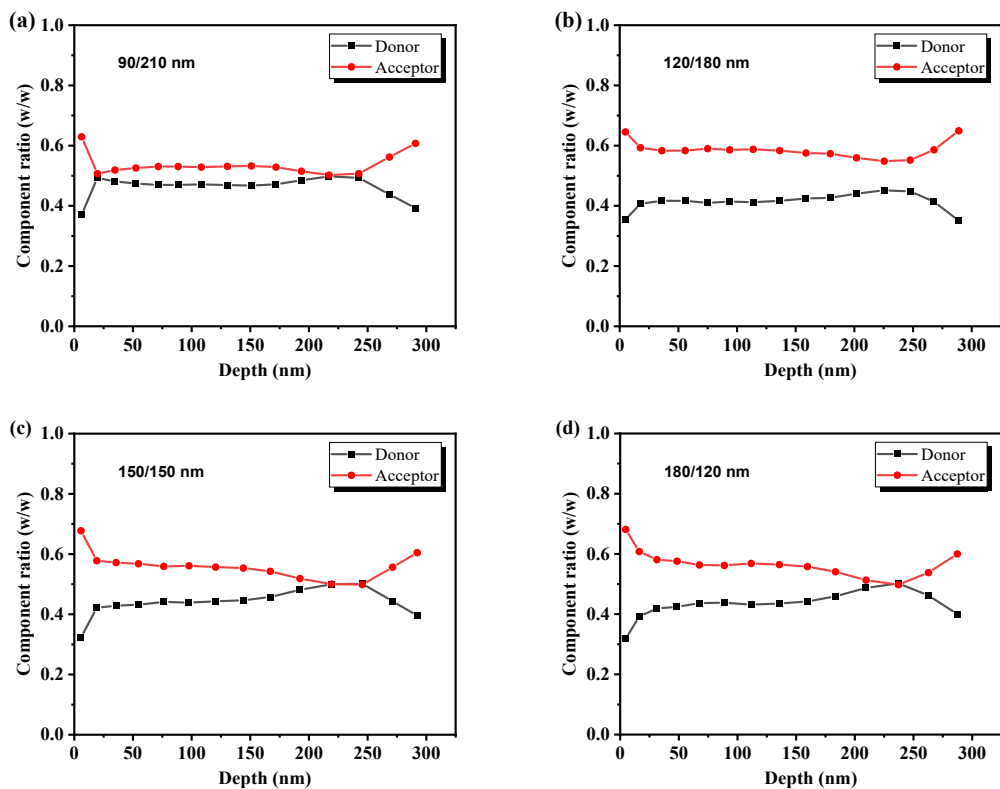
Supplementary Figure 29. The schematic morphology evolution for the layer-by-layer processed thick films.



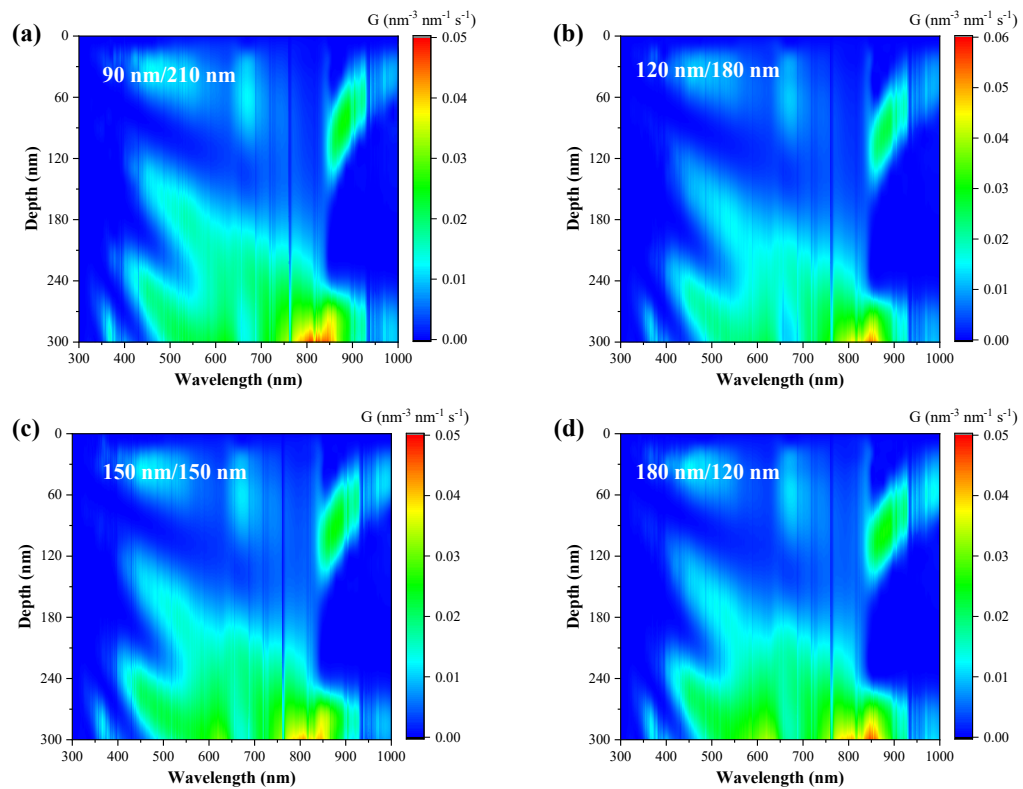
Supplementary Figure 30. Changes of normalized absorption intensity between 0.1 s and 60 s extracted from in-suit absorption spectra for PM6/L8-BO film fabricated with different donor and acceptor layer thicknesses.



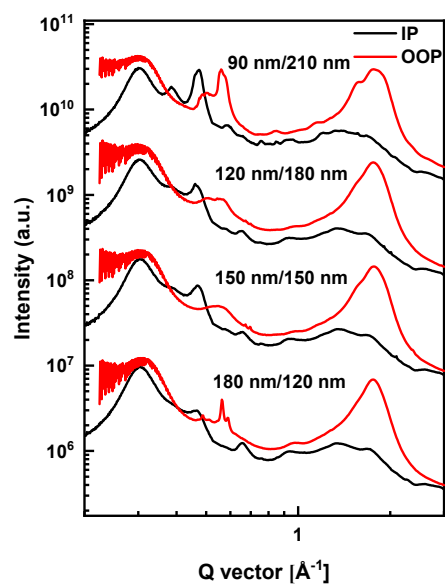
Supplementary Figure 31. Film-depth-dependent light absorption spectra of PM6/L8-BO blend films based on different donor and acceptor layer thicknesses.



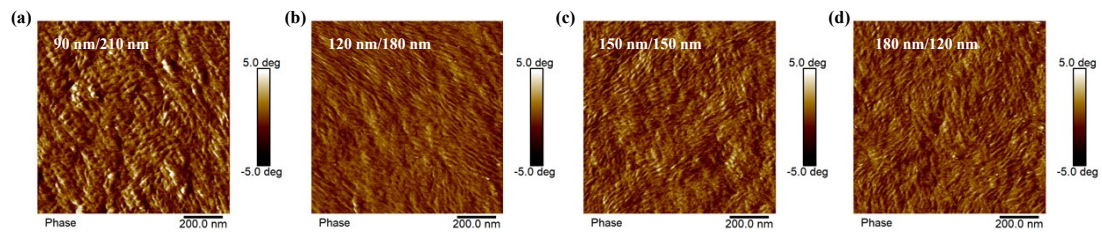
Supplementary Figure 32. The composition profiles extracted from the FLAS spectra of PM6/L8-BO blend films based on different donor and acceptor layer thicknesses.



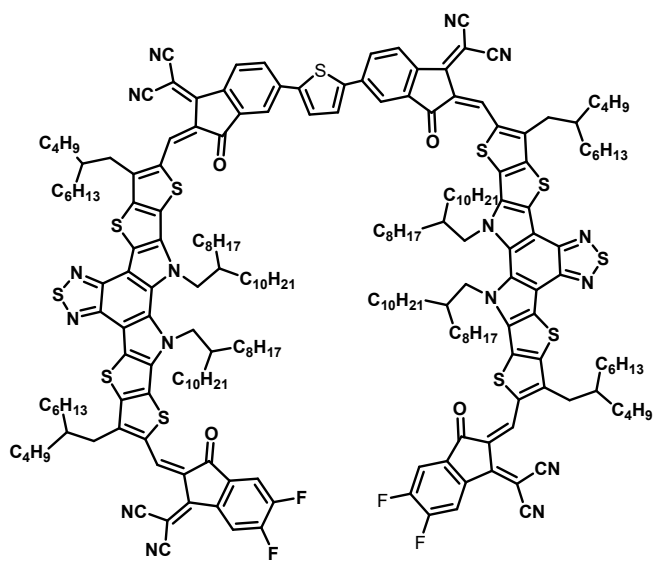
Supplementary Figure 33. Exciton generation contours of PM6/L8-BO blend films based on different donor and acceptor layer thicknesses.



Supplementary Figure 34. One-dimensional line curves of GIWAXS patterns with respect to the OOP and IP directions of PM6/L8-BO films with different donor and acceptor layer thicknesses.

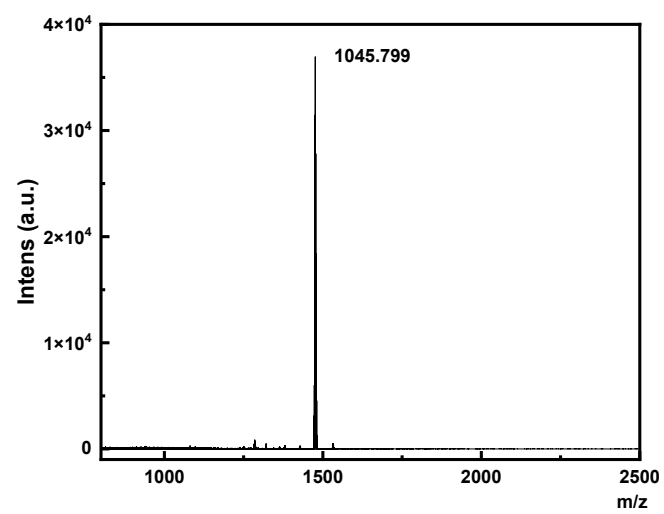


Supplementary Figure 35. AFM phase images of PM6/L8-BO film with different donor and acceptor layer thicknesses.

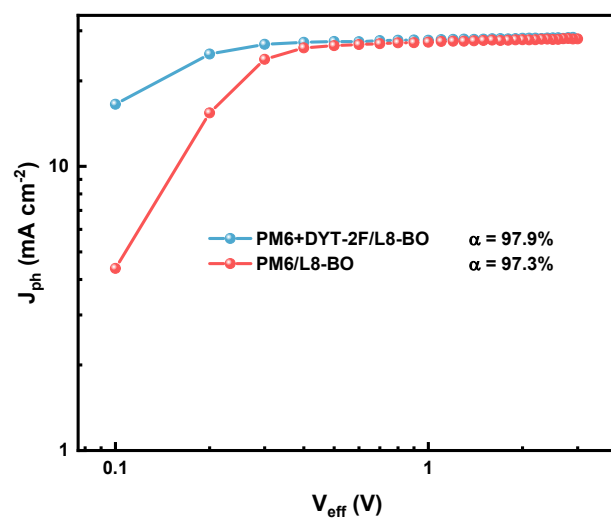


DYT-2F

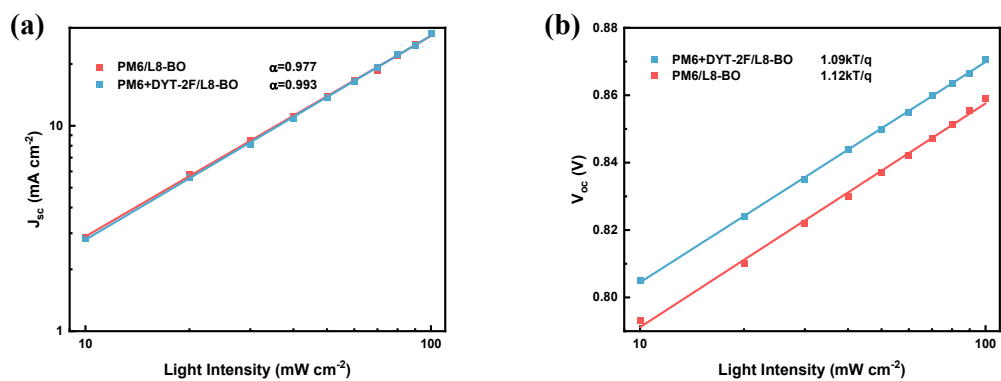
Supplementary Figure 36. Molecular structure of DYT-2F.



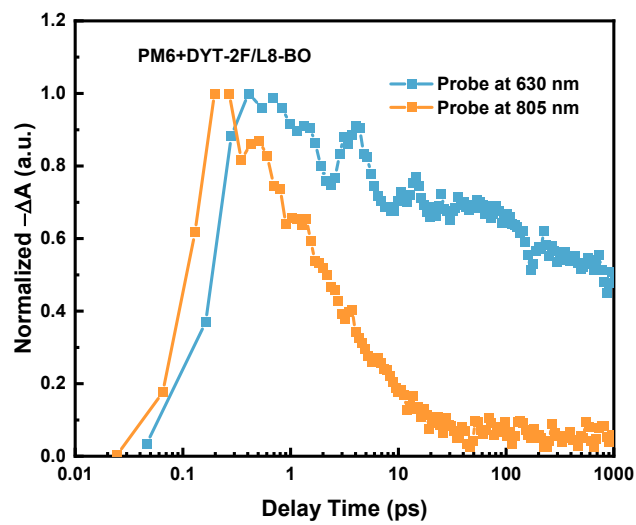
Supplementary Figure 37. MS (MALDI-TOF) spectrum of DYT-2F.



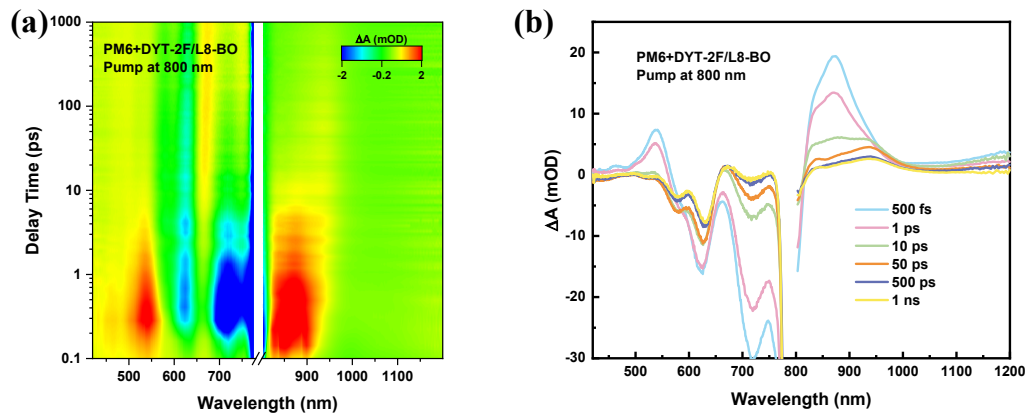
Supplementary Figure 38. The photocurrent density (J_{ph}) versus effective voltage (V_{eff}) characteristics of PM6/L8-BO devices with and without DYT-2F.



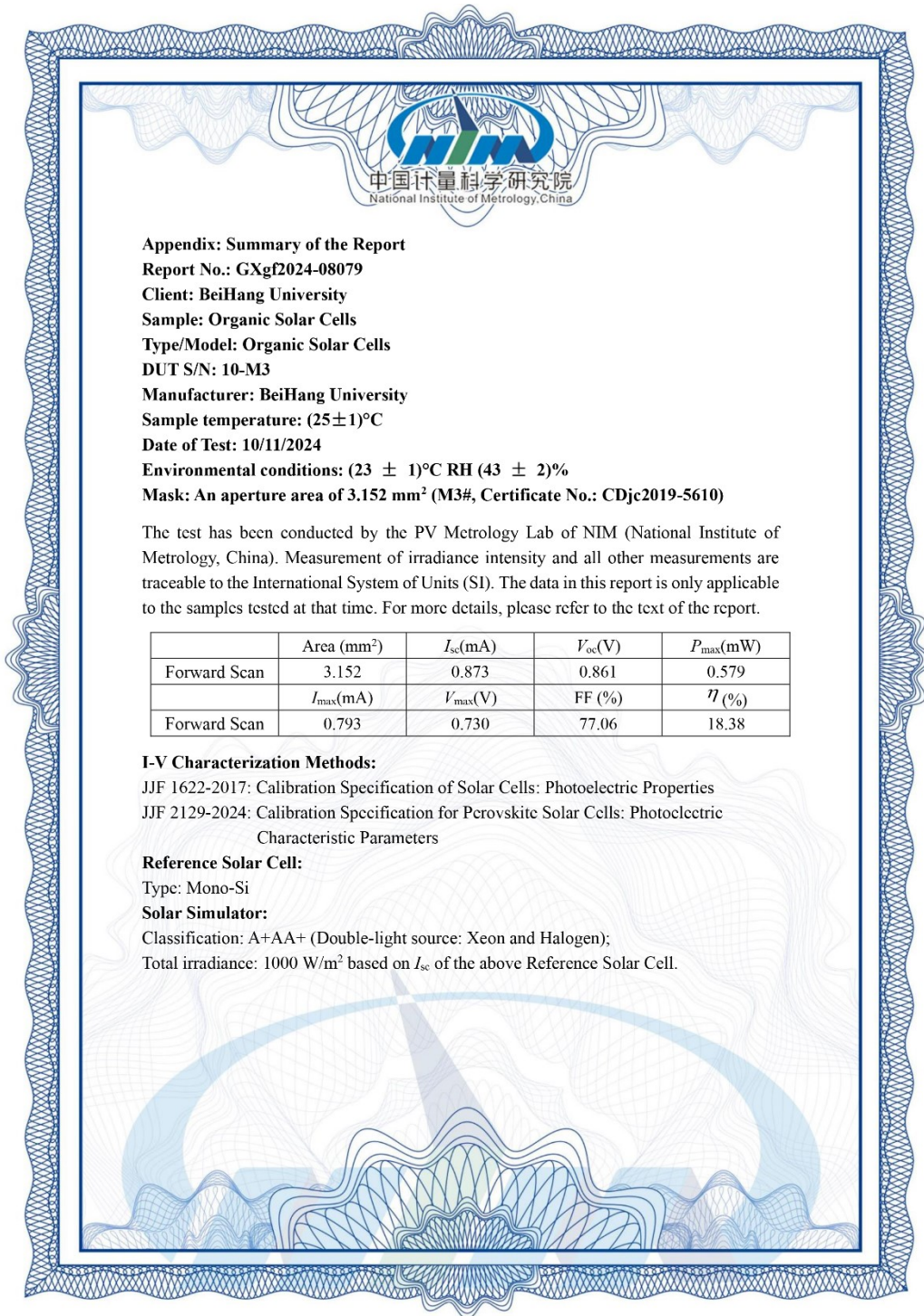
Supplementary Figure 39. (a) J_{sc} and (b) V_{oc} versus light intensity characteristics of PM6/L8-BO devices with and without DYT-2F.



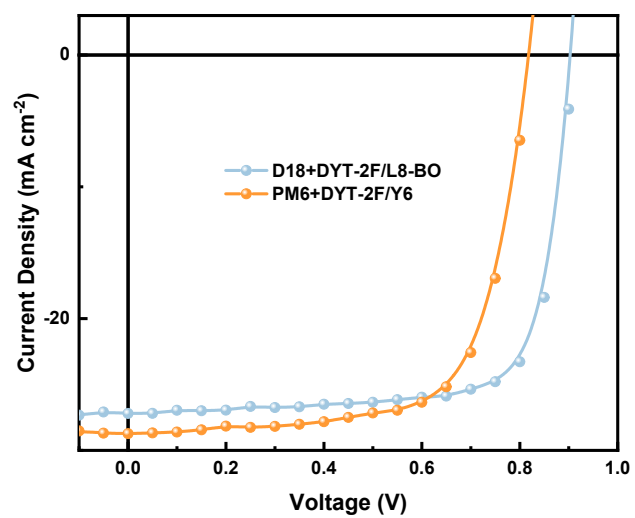
Supplementary Figure 40. Normalized TAS dynamic curves probed at 630 nm and 805 nm for PM6+DYT-2F/L8-BO thick films pumped at 800 nm.



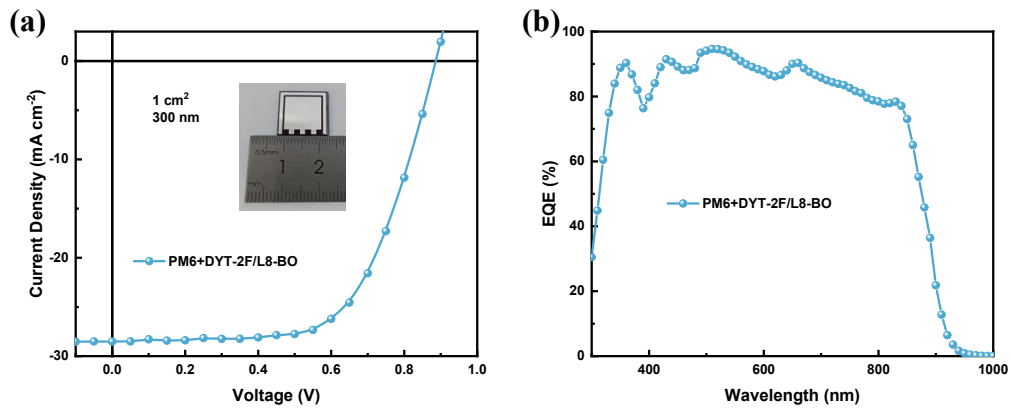
Supplementary Figure 41. (a) 2D TAS image and (b) the corresponding TAS spectra of PM6+DYT-2F/L8-BO thick film over time.



Supplementary Figure 42. Certification report of PM6+DYT-2F/L8-BO thick-film (300 nm) device by National Institute of Metrology (NIM), China.



Supplementary Figure 43. *J-V* curves of thick-film devices based on D18+DYT-2F/L8-BO and PM6+DYT-2F/Y6.



Supplementary Figure 44. (a) J - V curves and (b) corresponding EQE spectra for PM6+DYT-2F/L8-BO devices with large area (1 cm²).

Supplementary Table 1. Gaussian fitting parameters devices based on PM6/L8-BO with different donor and acceptor layer thicknesses.

Active layer	N_t ($\text{cm}^{-3} \text{eV}^{-1}$)	σ (meV)	E_t (eV)
90/210 nm	0.99×10^{17}	3.21	0.150
120/180 nm	1.32×10^{17}	4.50	0.152
150/150 nm	1.63×10^{17}	5.90	0.150
180/120 nm	1.77×10^{17}	6.46	0.150

Supplementary Table 2. Summary of photovoltaic parameters of thick-film OSC devices based on D18/L8-BO.

Active layer	V_{oc} (V)	J_{sc} (mA cm^{-2})	FF (%)	PCE ^{a)} (%)
D18/L8-BO (90 nm/210 nm)	0.889	26.21	75.7	17.56
	0.889 ± 0.001	25.96 ± 0.23	75.1 ± 0.2	17.33 ± 0.14
D18/L8-BO (120 nm/180 nm)	0.893	27.09	74.1	17.92
	0.890 ± 0.001	27.00 ± 0.17	73.8 ± 0.2	17.73 ± 0.10
D18/L8-BO (150 nm/150 nm)	0.889	27.32	71.8	17.44
	0.890 ± 0.001	27.09 ± 0.19	71.5 ± 0.3	17.25 ± 0.14
D18/L8-BO (180 nm/120 nm)	0.890	27.01	69.6	16.73
	0.890 ± 0.002	26.81 ± 0.21	69.3 ± 0.3	16.54 ± 0.13

a) Average values with standard deviation were obtained from 20 devices.

Supplementary Table 3. Summary of photovoltaic parameters of thick-film OSC devices based on PM6/Y6.

Active layer	V_{oc} (V)	J_{sc} (mA cm^{-2})	FF (%)	PCE ^{a)} (%)
PM6/Y6 (90 nm/210 nm)	0.811	28.28	66.6	15.27
	0.811 ± 0.002	28.03 ± 0.24	66.4 ± 0.1	15.10 ± 0.13
PM6/Y6 (120 nm/180 nm)	0.809	28.81	66.4	15.47
	0.809 ± 0.001	28.63 ± 0.15	66.3 ± 0.1	15.35 ± 0.08
PM6/Y6 (150 nm/150 nm)	0.813	29.19	65.2	15.47
	0.811 ± 0.002	28.92 ± 0.14	65.1 ± 0.1	15.26 ± 0.10
PM6/Y6 (180 nm/120 nm)	0.802	28.43	64.4	14.68
	0.805 ± 0.002	28.03 ± 0.29	64.2 ± 0.2	14.49 ± 0.15

a) Average values with standard deviation were obtained from 10 devices.

Supplementary Table 4. Summary of photovoltaic parameters of thick-film OSC devices with thickness of 500 nm.

Active layer	V_{oc} (V)	J_{sc} (mA cm ⁻²)	FF (%)	PCE ^{a)} (%)
PM6/L8-BO (150 nm/350 nm)	0.857	26.53	65.4	14.87
	0.857±0.001	26.31±0.14	65.3±0.2	14.72±0.09
PM6/L8-BO (200 nm/300 nm)	0.858	27.27	66.9	15.65
	0.858±0.001	27.10±0.21	66.7±0.1	15.50±0.12
PM6/L8-BO (250 nm/250 nm)	0.860	27.70	63.1	15.03
	0.859±0.001	27.23±0.46	62.8±0.2	14.70±0.25
PM6/L8-BO (300 nm/200 nm)	0.861	26.18	52.0	11.72
	0.859±0.002	25.84±0.27	51.9±0.2	11.52±0.12
D18/L8-BO (150 nm/350 nm)	0.875	26.26	66.4	15.26
	0.875±0.002	26.02±0.15	66.2±0.2	15.11±0.10
D18/L8-BO (200 nm/300 nm)	0.881	26.60	67.2	15.74
	0.880±0.001	26.44±0.18	67.0±0.2	15.58±0.17
D18/L8-BO (250 nm/250 nm)	0.881	26.91	64.2	15.22
	0.881±0.001	26.80±0.11	64.1±0.2	15.09±0.14
D18/L8-BO (300 nm/200 nm)	0.883	26.19	61.9	14.31
	0.882±0.001	25.88±0.22	61.3±0.3	14.05±0.21
PM6+DYT-2F/L8-BO	0.867	27.68	67.5	16.20
	0.867±0.001	27.48±0.44	67.1±0.3	15.97±0.23

a) Average values with standard deviation were obtained from 20 devices.

Supplementary Table 5. Global fitting parameters of L8-BO, PM6, and D18 neat films.

Materials	τ (ps)	k (s ⁻¹)	γ (cm ³ /s)	L_D (nm)
L8-BO	400	2.50×10^9	3.63×10^{-8}	24.04
PM6	210	4.76×10^9	2.83×10^{-8}	15.38
D18	143	6.99×10^9	5.60×10^{-8}	17.85

Supplementary Table 6. Summary of hole lifetimes and hole transfer rates based on different active layers.

Active layer	τ (ps)	k_{HT} ($\times 10^{10} \text{ s}^{-1}$)	η_{ht} (%)
L8-BO	5.17	/	/
PM6/L8-BO (90 nm/210 nm)	4.67	2.07	71.2
PM6/L8-BO (120 nm/180 nm)	4.45	3.13	69.2
PM6/L8-BO (150 nm/150 nm)	3.83	6.75	67.8
PM6/L8-BO (180 nm/120 nm)	2.98	14.20	62.1
PM6+DYT-2F/L8-BO	4.70	1.93	68.4

Supplementary Table 7. Summary of electron lifetimes and electron transfer rates based on different active layers.

Active layer	τ (ps)	k_{ET} ($\times 10^{10} \text{ s}^{-1}$)	η_{et} (%)
PM6	98.7	/	/
PM6/L8-BO (90 nm/210 nm)	42.3	1.35	57.1
PM6/L8-BO (120 nm/180 nm)	44.7	1.22	54.7
PM6/L8-BO (150 nm/150 nm)	47.1	1.11	52.2
PM6/L8-BO (180 nm/120 nm)	63.9	0.55	35.3
PM6+DYT-2F/L8-BO	42.0	1.37	57.5

Supplementary Table 8. Average electron and hole mobilities for PM6/L8-BO thick-film devices with different donor and acceptor layer thickness.

Active layer	Hole mobility μ_h ($10^{-4} \text{ cm}^2 \text{ V}^{-1} \text{ s}^{-1}$)	Electron mobility μ_e ($10^{-4} \text{ cm}^2 \text{ V}^{-1} \text{ s}^{-1}$)	μ_e/μ_h
90/210 nm	8.94	8.03	0.90
120/180 nm	8.36	9.34	1.12
150/150 nm	8.03	10.05	1.25
180/120 nm	8.02	11.17	1.39

Supplementary Table 9. Crystal Coherence lengths and the d-spacing for the PM6/L8-BO thick films with different donor and acceptor layer thickness.

	IP				OOP			
	q (\AA^{-1})	d -spacing (\AA)	FWHM (\AA^{-1})	CCL (\AA)	q (\AA^{-1})	d -spacing (\AA)	FWHM (\AA^{-1})	CCL (\AA)
90/210 nm	0.304	20.66	0.077	73.44	1.774	3.54	0.507	11.15
120/180 nm	0.301	20.87	0.076	74.41	1.764	3.56	0.454	12.45
150/150 nm	0.300	20.94	0.076	74.41	1.762	3.57	0.445	12.71
180/120 nm	0.300	20.94	0.075	75.40	1.754	3.58	0.430	13.15

Supplementary Table 10. Summary of photovoltaic parameters of thick-film OSC devices based on D18+DYT-2F/L8-BO and PM6+DYT-2F/Y6.

Active layer	V_{oc} (V)	J_{sc} (mA cm^{-2})	FF (%)	PCE ^{a)} (%)
D18+DYT-2F/L8-BO	0.907	27.20	75.5	18.63
	0.906±0.001	27.06±0.20	75.3±0.2	18.48±0.10
PM6+DYT-2F/Y6	0.819	28.73	69.5	16.35
	0.818±0.001	28.53±0.19	69.4±0.2	16.19±0.10

a) Average values with standard deviation were obtained from 20 devices.

Supplementary Table 11. Summary of photovoltaic performance parameters of thick-film OSCs.

Thickness system	Thickness (nm)	PCE (%)	References
PM6:Y6	300	13.60	[1]
PM6:Y6	250	14.1	[1]
PM7:MF1	312	12.03	[2]
PM7:MF1	445	11.11	[2]
PM7:MF1	510	10.07	[2]
PM7:MF2	308	12.34	[2]
PM7:MF2	438	11.04	[2]
PM7:MF2	500	10.04	[2]
PM6:BP4T-4F:BP3T-4F	300	16.03	[3]
PM6: Y6:BTP-M	300	14.23	[4]
PM6:BTP-eC9	300	16.25	[5]
PM6:BTP-eC9	400	15.12	[5]

PM6:BTP-eC9	500	14.37	[5]
D18:Y6:PC61BM	300	16.32	[6]
PM6:BTP-eC9:L8-BO-F	300	17.31	[7]
D18:BTR-Cl:Y6	308	15.50	[8]
Si25:Y14	430	15.39	[9]
Si25:Y14	600	15.03	[9]
PBDB-T-2Cl:BP-4F:MF1	300	14.57	[10]
PM6:F-2Cl	263	12.29	[11]
PM6:F-2Cl	519	11.41	[11]
PM6:BTP-eC9:L8-BO:BTP-S10	305	17.55	[12]
D18:ZW1:Y6	200	17.83	[13]
D18:ZW1:Y6	250	17.61	[13]
D18:ZW1:Y6	293	16.67	[13]
D18:ZW1:Y6	493	15.56	[13]
PM6:L8-BO	300	17.80	[14]
PM6:αBTCI:L8-BO	330	17.46	[15]
PM6:L8-BO:DY-TF	300	18.23	[16]
PM6:L8-BO	305	17.53	[17]
PM6+PS:L8-BO	300	18.15	[18]
D18:L8-BO	500	16.00	[19]
D18:L8-BO	220	17.70	[19]
D18:L8-BO	300	16.90	[19]
D18:L8-BO	400	16.30	[19]
PM6+DYT-2F/L8-BO	300	18.92	Thick work
PM6+DYT-2F/L8-BO	500	16.20	Thick work

Reference

- [1] J. Yuan, Y. Zhang, L. Zhou, G. Zhang, H.-L. Yip, T.-K. Lau, X. Lu, C. Zhu, H. Peng, P. A. Johnson, M. Leclerc, Y. Cao, J. Ulanski, Y. Li, Y. Zou, *Joule* 2019, 3, 1140.
- [2] W. Gao, Q. An, M. Hao, R. Sun, J. Yuan, F. Zhang, W. Ma, J. Min, C. Yang, *Adv. Funct. Mater.* 2020, 30, 1908336.
- [3] J. Gao, W. Gao, X. Ma, J. Wang, X. Wang, C. Xu, X. Zhang, J. Zhang, C. Yang, A. K.-Y. Jen, F. Zhang, *Sol. RRL* 2021, 5, 2100365.
- [4] L. Zhan, S. Li, T.-K. Lau, Y. Cui, X. Lu, M. Shi, C.-Z. Li, H. Li, J. Hou, H. Chen, *Energy Environ. Sci.* 2020, 13, 635.
- [5] Y. Zhang, K. Liu, J. Huang, X. Xia, J. Cao, G. Zhao, P. W. K. Fong, Y. Zhu, F. Yan, Y. Yang, X. Lu, G. Li, *Nat. Commun.* 2021, 12, 4815.
- [6] J. Qin, L. Zhang, Z. Xiao, S. Chen, K. Sun, Z. Zang, C. Yi, Y. Yuan, Z. Jin, F. Hao, Y. Cheng, Q. Bao, L. Ding, *Sci. Bull.* 2020, 65, 1979.
- [7] Y. Cai, Q. Li, G. Lu, H. S. Ryu, Y. Li, H. Jin, Z. Chen, Z. Tang, G. Lu, X. Hao, H. Y. Woo, C. Zhang, Y. Sun, *Nat. Commun.* 2022, 13, 2369.
- [8] H. Zhao, B. Lin, J. Xue, H. B. Naveed, C. Zhao, X. Zhou, K. Zhou, H. Wu, Y. Cai, D. Yun, Z. Tang, W. Ma, *Adv. Mater.* 2022, 34, 2105114.
- [9] F. Pan, M. Luo, X. Liu, H. Jiang, Z. Wang, D. Yuan, Q. Wang, L. Qing, Z. Zhang, L. Zhang, Y. Zou, J. Chen, *J. Mater. Chem. A* 2021, 9, 7129.
- [10] J. Gao, W. Gao, X. Ma, Z. Hu, C. Xu, X. Wang, Q. An, C. Yang, X. Zhang, F. Zhang, *Energy Environ. Sci.* 2020, 13, 958.
- [11] Y. Zhang, H. Feng, L. Meng, Y. Wang, M. Chang, S. Li, Z. Guo, C. Li, N. Zheng, Z. Xie, X. Wan, Y. Chen, *Adv. Energy Mater.* 2019, 9, 1902688.
- [12] L. Zhan, S. Yin, Y. Li, S. Li, T. Chen, R. Sun, J. Min, G. Zhou, H. Zhu, Y. Chen, J. Fang, C. Q. Ma, X. Xia, X. Lu, H. Qiu, W. Fu, H. Chen, *Adv. Mater.* 2022, 34, 2206269.
- [13] W. Zou, C. Han, X. Zhang, J. Qiao, J. Yu, H. Xu, H. Gao, Y. Sun, Y. Kan, X. Hao, G. Lu, Y. Yang, K. Gao, *Adv. Energy Mater.* 2023, 2300784.
- [14] X. Song, H. Xu, X. Jiang, S. Gao, X. Zhou, S. Xu, J. Li, J. Yu, W. Liu, W. Zhu, P. Müller-Buschbaum, *Energy Environ. Sci.*, 2023,16, 3441-3452.
- [15] C. Zhang, J. Li, W. Deng, J. Dai, J. Yu, G. Lu, H. Hu, K. Wang, *Adv. Funct. Mater.* 2023, 33, 2301108.
- [16] Y. Wei, Y. Cai, X. Gu, G. Yao, Z. Fu, Y. Zhu, J. Yang, J. Dai, J. Zhang, X. Zhang, X. Hao, G. Lu, Z. Tang, Q. Peng, C. Zhang, H. Huang, *Adv. Mater.* 2024, 36, 2304225.
- [17] Z. Ge, J. Qiao, J. Song, X. Li, J. Fu, Z. Fu, J. Gao, X. Tang, L. Jiang, Z. Tang, G. Lu, X. Hao, Y. Sun, *Adv. Energy Mater.* 2024, 2400203.
- [18] Z. Fu, J. Qiao, F. Cui, W. Zhang, L. Wang, P. Lu, H. Yin, X. Du, W. Qin, X. Hao, *Adv. Mater.* 2024, 36, 2313532.
- [19] H. Zhang, Y. Liu, G. Ran, H. Li, W. Zhang, P. Cheng, Z. Bo, *Adv. Mater.* 2024, 2400521